Query Details

Back to Main Page

1. The given sentence 'Although the three fitting peaks of high-resolution ...' seems to be incomplete. Please check for missing words/phrases and complete the sentence.

Checked

2. We have deleted the part lable (A) in the citation of Fig. 1. Please check and confirm.

Checked

3. Please provide the part lables (a, B) explanation of Figs. 4, 6, and 8 within the figure caption to correspond with the image.

Checked

4. The given sentence 'Although TiO2...at the fifth recycling run.' seems to be incomplete. Please check for missing words/phrases and complete the sentence.

checked

5. As References [1] and [43] are same, we have deleted the duplicate reference and renumbered accordingly. Please check and confirm.

Checked

6. As References [2] and [51] are same, we have deleted the duplicate reference and renumbered accordingly. Please check and confirm.

Checked, Thank you

Fabrication of visible-light-responsive TiO_2/α-Fe_2O_3-heterostructured composite for rapid photo-oxidation of organic pollutants in water

S. Kavitha Affiliationids : Aff1

R. Ranjith Affiliationids : Aff2

N. Jayamani

Email : jayamaniphysics@gmail.com

Affiliationids : Aff1, Correspondingaffiliationid : Aff1

S. Vignesh Affiliationids : Aff3

Baskaran Palanivel Affiliationids : Aff4

R. Djellabi Affiliationids : Aff5

C. L. Bianchi

Email : claudia.bianchi@unimi.it

Affiliationids : Aff5, Correspondingaffiliationid : Aff5

Fahad A Alharthi Affiliationids : Aff6

Aff1 PG & Research Department of Physics, Government Arts College (Autonomous), Tamil Nadu, 636007, Salem, India

Aff2 Annai Arts and Science College, Nambipatti, Harur, Tamil Nadu, 636903, Dharmapuri, India

Aff3 SSN Research Centre, Sri Sivasubramaniya Nadar (SSN) College of Engineering, Kalavakkam, 603110, Chennai, Tamil Nadu , India

Aff4 Department of Physics and Nanotechnology, SRM Institute of Science and Technology, Chengalpattu, Tamil Nadu, 603203, India

Aff5 Department of Chemistry, Università degli Studi di Milano, 20133, Milano, Italy

Aff6 Department of Chemistry, College of Science, King Saud University, Riyadh, 11451, Saudi Arabia

Received: 20 July 2021 / Accepted: 3 September 2021

Abstract

In this present work, a visible-light-responsive TiO_2/α-Fe_2O_3-heterostructured nanocomposite was fabricated by hydrothermal and ultrasonication methods. To unravel the physicochemical and optical characteristics, the as-fabricated photocatalysts were

characterized by PXRD, FT-IR, HRSEM, HRTEM, UV–Vis DRS absorption, and PL analysis, respectively. The optical band gap (E_g) of TiO_2 and TiO_2/α-Fe_2O_3 were found to be 3.21 and 2.72 eV, respectively. The photocatalytic efficiency of TiO_2/α-Fe_2O_3 composite photocatalyst was evaluated towards the degradation of aqueous methylene blue (MB) dye under visible-light irradiation. The results showed that the heterostructured α-Fe_2O_3/TiO_2 catalyst exhibits faster and higher removal efficiency of (20 ppm) MB dye (92.7%) than the other photocatalytic degradation of pristine TiO_2 (33%) and α-Fe_2O_3 (47.3%) within 100 min. The enriched photocatalytic efficiency is due to the enhanced visible-light response following by interfacial charges transfer between TiO_2 and α-Fe_2O_3 which in turn allows the formation of a high yield of separated electron–hole (e^-/h^+) pairs and produced of reactive oxygen species. On top of the enhanced photoactivity, TiO_2/α-Fe_2O_3 showed great stability and recycling ability which may encourage its transfer to real use towards the purification of wastewater.

1. Introduction

For better water worldwide supply and environmental remediation, the effective elimination of toxic compounds from wastewaters before discharging them has become an imperative and a major global concern. Nowadays, with the rapid industrialization of modern society exclusively in developing countries, organic dyes are widely used in different industrial processing including paper, leather, textile, pigment, cosmetic, food, and drug manufacturing [1, 2, 3]. Besides, industrial and sanitary sewage comprises dyes that cause water contamination as serious health problems, and they are hazardous effects on aquatic organisms, plants, humans, animals, and the aquatic ecosystem. Various techniques have been adopted from the former few decades to treat dye-containing waters such as advanced oxidation processes (AOPs), physical adsorption, ozonation, photolysis, and biological decomposition [3, 4]. Among them, semiconductors (SCs) heterogeneous photocatalytic AOPs decomposition has been expected to be an effective strategy for used by many researchers because of its high degradation/mineralization efficiency to remove organic pollutants from wastewater due to the photogenerated reactive oxygen species (ROSs, e.g., $^{\bullet}OH$), also low toxicity, low cost, and ability to work under ambient settings [5].

Among various semiconductor photocatalysts (PCs), the well-known Titania (TiO_2) has attracted extensive courtesy owed to their preponderant potential features such as low cost, non-toxicity, high photo-stability, acceptable electronic assets, excellent photochemical corrosive resistance, strong oxidizing power, and photocatalytic movement [6, 7, 8]. This is based on the absorption of a photon of appropriate energy (~ 3.2 eV) and the creation of charge carriers [photo-electrons (e^-) and photo-holes (h^+)] that can produce ROSs for the oxidation of organic pollutants into CO_2 and H_2O. However, the practical application of TiO_2 catalyst is hindered by the severe agglomeration of TiO_2 nanoparticles (NPs) and the quick recombination of the photo-produced (e^-/h^+) pairs [9, 10]. Moreover, the wide band gap of TiO_2 limits its photocatalytic property in the ultraviolet (UV) region, which accounts for 3–5% of the total solar-light proportion spectrum. Since utilizing the visible light is much more abundant (~ 43%) than UV light in the solar source; hence, its efforts to synthesize efficient visible-light-responsive TiO_2-based PCs are highly desired [11]. Several methods employed for enlightening the photocatalytic activity, the tremendous efforts are going to develop visible-light-driven (VLD) semiconductor PCs with heterojunction architecture for the TiO_2 PCs were coupled with various narrower band-gap SCs, such as CeO_2, WO_3, g-C_3N_4, MoS_2, GO, Cu_2O, Fe_2O_3, and CdS [11, 12, 13, 14, 15, 16].

Among diverse metal-oxides (MOs) semiconductor PCs, hematite (α-Fe_2O_3) is a kind of typical n-type SCs that also facilitate the promising photocatalytic water splitting and water treatment applications. Because of its narrow band gap (~ 2.0–2.2 eV), which exhibits excellent properties such as non-toxicity, environmentally friendly, natural abundance, superior chemical steadiness, good conductivity, better visible-light fascination ability, and solid oxidation power [17]. To resolve this inadequacy, it is an attractive route to organize the effective PCs by incorporating magnetic α-Fe_2O_3, which prevents the agglomeration of other NPs during recovery and deals with the synergetic enrichment of catalytic activity to some extent by forming a hybrid structure [18]. Nevertheless, the photo-produced (e^-/h^+) pairs in the valence band (VB) and conduction band (CB) of α-Fe_2O_3 are easier to be excited under visible-light exposure [19]. Besides, the coupling between α-Fe_2O_3 and TiO_2 NPs forms the most promising nanostructures (NSs) that could support the spatial electron (e^-) transfer, preventing the recombination of e^-/h^+ pairs and supplying more reaction active sites for widely improve the photocatalytic performance and recycling uses. Therefore, band bending might occur that the CB edge of α-Fe_2O_3 is higher than TiO_2 when their Fermi levels are equalized [17]. As well, α-Fe_2O_3 ions particularly adsorb on the negatively charged TiO_2 NPs by electrostatic dealings. Also, modifying their band structures via unique properties of α-Fe_2O_3 makes a suitable aspirant for coupling with TiO_2 would progress a new energy-level mismatch for visible-light photocatalysis. Therefore, α-Fe_2O_3 is extensively used as combined for VLD TiO_2-based PCs by the hydrothermal-assisted technique with the ultrasonic wave's supports. Since hydrothermal-assisted precipitation has applied the most effective route among various techniques to fabricate the effectual NPs and nanocomposites (NCs) samples due to its high purity, simple preparation, stoichiometry control, and homogeneous distribution of coupling components [20]. Fortunately, magnetic PCs might be proficiently separated and reprocessed by applying an external magnetic field [21].

In the present work, TiO_2/α-Fe_2O_3 heterojunction photocatalyst was synthesized by facile hydrothermal-assisted precipitation followed by ultrasonic dispersion. Various physicochemical and optical characterizations were recorded on the as-fabricated NCs. The photoactivity of as-prepared materials was checked towards the oxidation of MB under visible light. Based on the results of materials characterization and the photoactivity comparison between bare photocatalysts and TiO_2/α-Fe_2O_3 composite, the mechanistic pathways towards MB oxidation under visible light were suggested.

2. Experimental

2.1. Materials and reagents

Sodium hydroxide (NaOH) was obtained from Pure Chem Chemical Co., India. Titanium (IV) isopropoxide [TTIP, Ti $(OC_4H_9)_4$ 98.5%]

[$C_{16}H_{21}NO_2$, 98%], and Ethanol Absolute (C_2H_6O, 96%) were attained from Merck Chemical Co., India. Entire chemicals were used here in analytical reagent (A.R) grade without auxiliary refinement, and reaction solutions formed with high-purity deionized (D.I.) water.

2.2. Photocatalysts synthesis

The pristine TiO_2 NPs was fabricated by facile sol–gel process. Initially, the typical 5 mL of TTIP was added into 30 mL of 2-propanol solution. Then, the 0.1 g of PVP mixed with 20 mL of D.I. water was openly added to the solution magnetically stirred for 60 °C at 4 h; next it was transferred to Teflon-lined autoclave for 140 °C at 8 h. Finally, the harvested TiO_2 NPs were washed and further dried at 70 °C overnight, and then crushed gently with mortar to acquire TiO_2 NPs [22]. The α-Fe_2O_3 NPs was prepared via a precipitation route. In a typical experiment, 0.1 M $FeCl_3$. $6H_2O$ and 0.1 g of PVP were dissolved in 100 mL of D.I. water and 50 mL of absolute ethanol solution composed under continuous vigorous stirring for 1 h at a temperature of 70 °C. Next, the aqueous ammonia solution was slowly added dropwise into beyond colloidal suspensions to adjust the pH ~ 11 and subsequently aged at 60 °C. After naturally cooling at room temperature, the resultant dark red precipitates were obtained, which were collected by centrifugation (3000 rpm), rinsed with D.I. water and ethanol to remove excess chlorine ions from the filtered material [23]. The obtained wet precipitous was then dried for 10 h at 80 °C and then calcined in air at 750 °C for 3 h to obtain α-Fe_2O_3 NPs.

The TiO_2/α-Fe_2O_3 composite sample was fabricated by facile approach: As-fabricated TiO_2 and α-Fe_2O_3 NPs were dispersed into ethanol and intensively sonicated for 30 min by probe ultrasonication. The resulting mixed suspension was subjected to furnace calcination at 450 °C for 5 h, hence to attain TiO_2/α-Fe_2O_3 composite in powder form [24, 25].

2.3. Characterization

Powder X-ray diffraction (XRD) analysis was passed out to define the crystal structure and phase of the as-fabricated PCs by Rigaku Miniflex II X-ray diffractometer, which was a Cu Kα radiation (λ = 1.54056 Å). Fourier-transform infrared (FT -IR) spectra were noted on a Perkin Elmer RX-1 spectrometer via a KBr pellet method in the ranges of 4000–400 cm^{-1} for exploring the functional features. To identify surface morphologies and elemental configuration (weight %), high-resolution scanning electron microscope images, including energy dispersive X-ray spectra (EDXS), were documented through HRSEM; FEI Quanta FEG 200. The shape and deep microstructure were advance categorized by high-resolution transmission electron microscopy (HRTEM) analysis consuming a JEOL/JEM 2100, operated at an accelerating voltage of 200 kV. UV–Vis diffuse reflectance spectroscopy (UV–Vis DRS) analysis attained the optical absorption spectra on a UV2550; Shimadzu device. The room-temperature photoluminescence (PL) spectral analysis was conceded out using a Perkin-Elmer-LS 100 by the excitation wavelength series on λ_{ex} = ~ 330 nm.

2.4. Photocatalytic activity

The photocatalytic activities of as-fabricated catalysts were evaluated towards the photodegradation of MB (20 ppm) in the presence of 50 mg in 100 mL of the cylindrical quartz reflux system. The mixture was stirred in dark for 30 min to realize adsorption–desorption equilibrium. Then, the visible light (300 W Xe lamp equipped with a cutoff filter of $\lambda > 420$ nm) was turned on to initiate the photocatalytic degradation. Each 20 min, 2 mL of MB solution was taken to remain the concentration by UV–Vis spectra (Perkin Elmer-Lambda 35) at 664 nm [26]. The photodecomposition removal efficiency rate % of MB was calculated using the following equation: $\text{Efficiency } (\%) = (C_0 - C_t)/C_0 * 100$. In addition, the dye elimination kinetics were followed using the equation of linear pseudo-first-order relation model: $-\text{Ln}(C_0/C_t) = kt$. Wherever C_t was the absorption found to MB dye in the preferred time intervals, k stands for the dye removal pseudo-first-order rate constant, C_0 has the initial absorbance of the MB dye at t = 0 min, and relative time t [27, 28]. The recycling experiments were carried out under the same conditions, after washing and drying the photocatalyst after each use.

3. Results and discussion

Figure 1 illustrates the XRD pattern of as-fabricated pristine TiO_2, α-Fe_2O_3, and TiO_2/α-Fe_2O_3 composite samples. Crystalline planes consistent with the peaks for TiO_2 and α-Fe_2O_3 are well indexed in Fig. 1. Numerous characteristic crystalline peaks sensed for pristine TiO_2 sample at 2θ = 25.2°, 38.4°, 48.2°, 53.9°, 55.2°, and 62.8° indexed to the (101), (112), (200), (105), (211), and (213) crystalline planes signifying the presence of only prime TiO_2 tetragonal anatase crystallization phase (JCPDS file no. 21-1272) [18, 29]. Conversely, minor peaks are noticed at around 27.4° owed to the presence of a slight portion of the TiO_2 rutile phase. On the other hand, main diffraction peaks at 24.3°, 35.4°, 40.7°, and 54.23° could be consigned to (012), (110), (113), and (116) crystal planes in the best contract (JCPDS file no. 01-1053) with rhombohedral hematite α-Fe_2O_3 phase, relatively. Moreover, the intensity of (101) peak was increased in the TiO_2/α-Fe_2O_3 composite when compared to bare TiO_2, while the diffraction planes may overlap the α-Fe_2O_3. Accordingly, the XRD outcomes showed that α-Fe_2O_3 NPs was effectively formed on the surface of TiO_2. No further impurity peaks were detected, suggesting the formation of pure TiO_2/α-Fe_2O_3 heterojunction composite [30]. The average crystallite size of as-fabricated pristine TiO_2, α-Fe_2O_3, and TiO_2/α-Fe_2O_3 catalysts were estimated by the Scherrer Eq. [1] and the obtained values are 31, 19, and 24 nm, respectively. The crystalline size has been reduced because the lattice distortion might be caused by ionic radius differences among the TiO_2 and α-Fe_2O_3 NPs [31].

Fig. 1

Powder XRD pattern of as-obtained samples

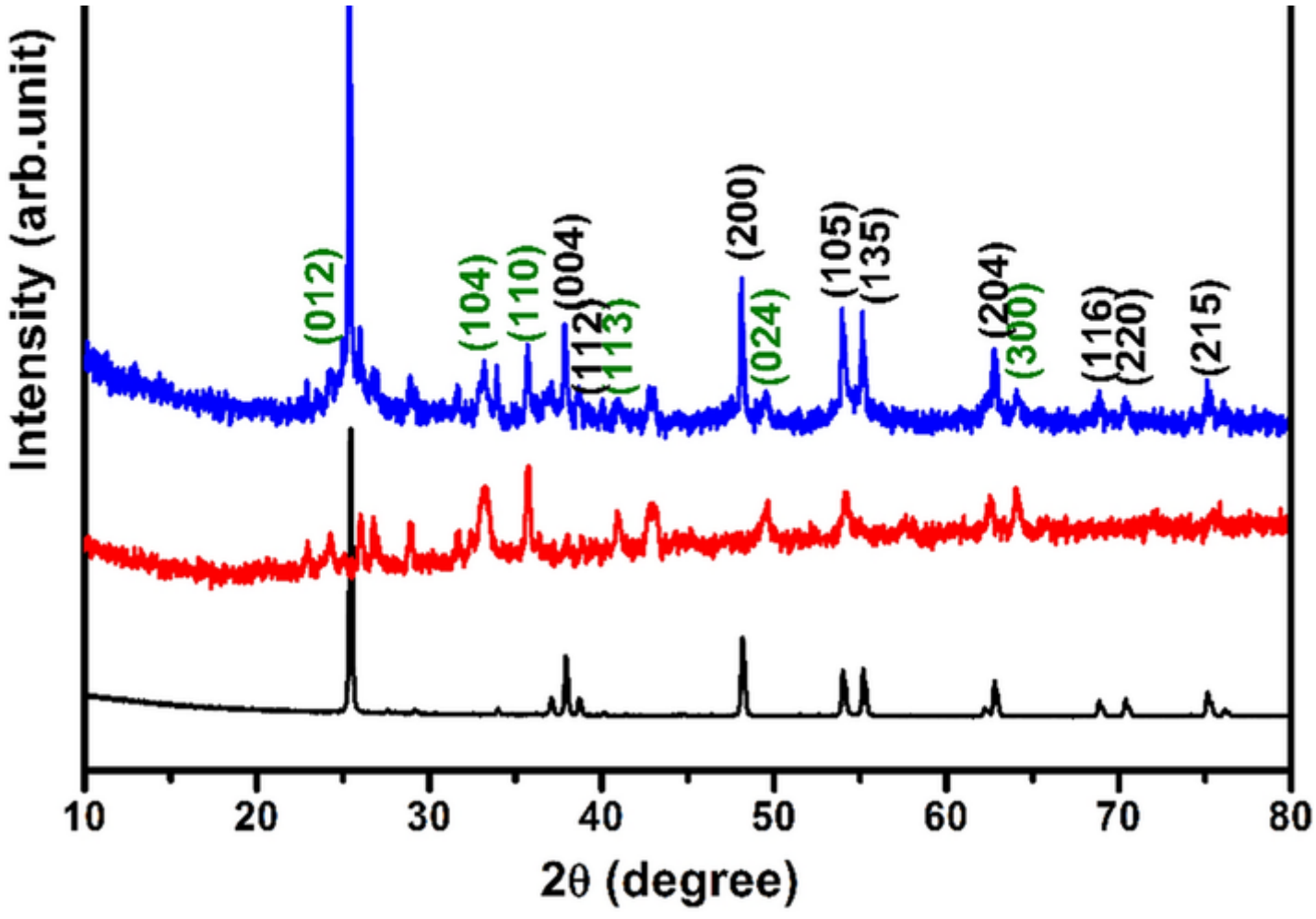

The FT-IR spectra were recorded to check the chemical bonding of the as-prepared photocatalysts. Figure 2 displays the FT-IR spectra for as-fabricated pristine TiO_2, α-Fe_2O_3, and TiO_2/α-Fe_2O_3 composite. The huge band below 800 cm^{-1} (in bare TiO_2, and also TiO_2/α-Fe_2O_3) is due to the Ti–O–Ti vibrational modes [32]. The α-Fe_2O_3 spectrum exhibits two peaks at around 460 and 565 cm^{-1} which are due to stretching vibrations of Fe–O [31]. The peaks at around 1500 cm^{-1} are due to C–O and C–C vibrations due to the presence of PVP, which was added during the synthesis [33]. The absorption peaks in the region of 2830–2980 cm^{-1} agree to CH vibrations (from PVP). The typical extensive absorptive peak produced at 1632 and 3451 cm^{-1} are attributed to OH bending and stretching vibrations that appeared from the adsorbed water molecules [34].

Fig. 2

FT-IR spectra of as-obtained samples

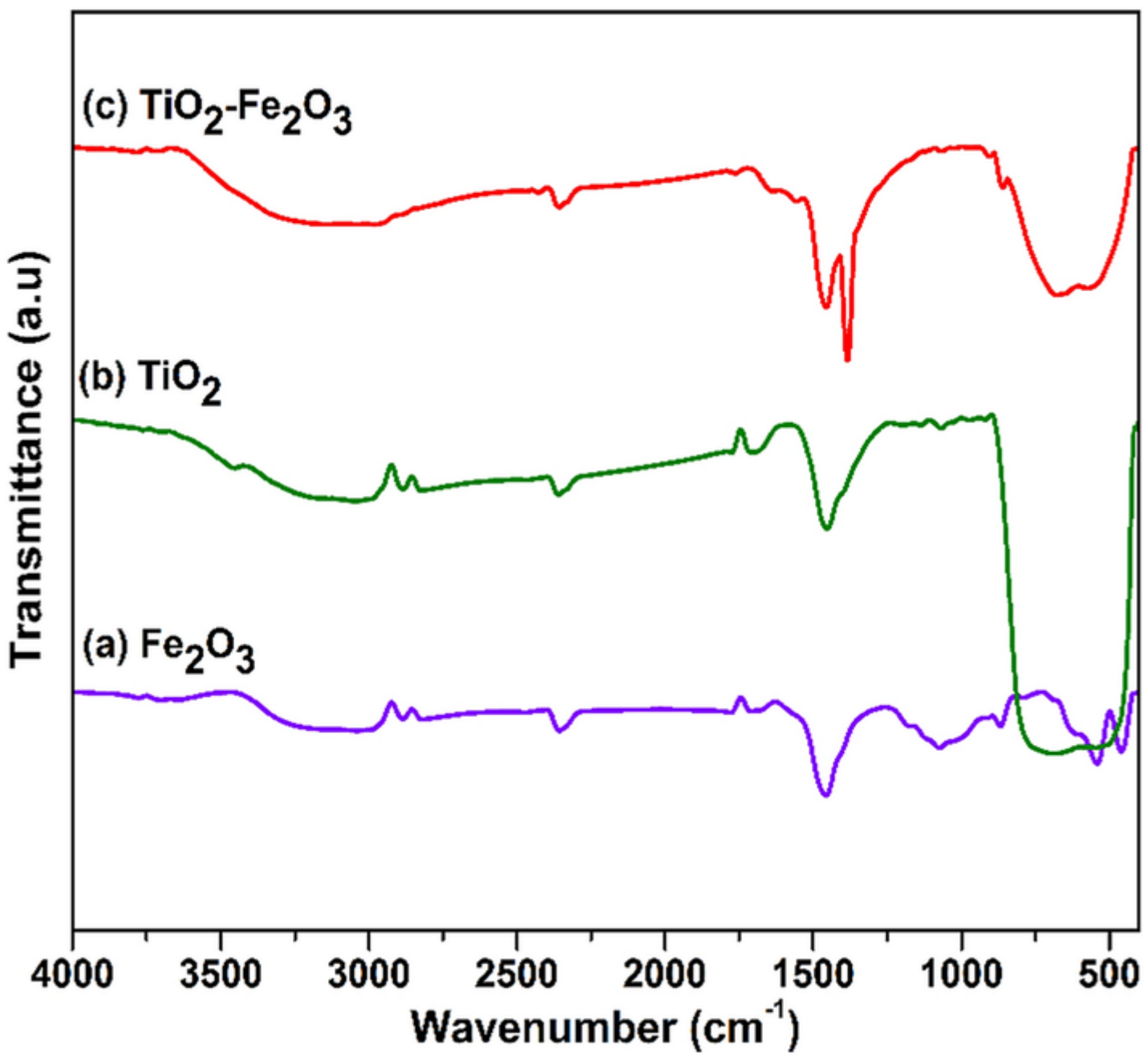

Figure 3 a exhibits the HRSEM image of pristine TiO_2 NPs, wherein it can be seen that in which TiO_2 NPs show an irregularly shaped morphology. In Fig. 3 b, it is observed that the pristine α-Fe_2O_3 NPs are composed of a flake-like structures morphology and copious agglomerated certain dispersed NPs. Also, it is observed in TiO_2/α-Fe_2O_3 catalyst composite (Fig. 3 c) that the flake-like nanostructured α-Fe_2O_3 materials were self-possessed on the surface of TiO_2 assembly and fairly agglomerated with randomly distributed, which would be beneficial for augmenting the catalytic activity [2, 35]. Besides, the EDXS spectrum was used to conclude the elemental weight ratio for the TiO_2/α-Fe_2O_3 composite sample as shown in Fig. 3 d. The results show (inset Fig. 3 d) that the O, Ti, and Fe elements were 42.11%, 40.15%, and 17.74% (weight %), respectively. The EDXS element mapping images (Fig. 4 a–d) of TiO_2/α-Fe_2O_3 composite for auxiliary confirm the spatial distribution and the pinpointed/isolated spots of the O, Fe, and Ti elements [5, 36].

Fig. 3

HRSEM images of as-fabricated **a** pristine TiO_2 **b** α-Fe_2O_3 **c** TiO_2/α-Fe_2O_3 composite and **d** consistent EDXS spectrum of TiO_2/α-Fe_2O_3 composite

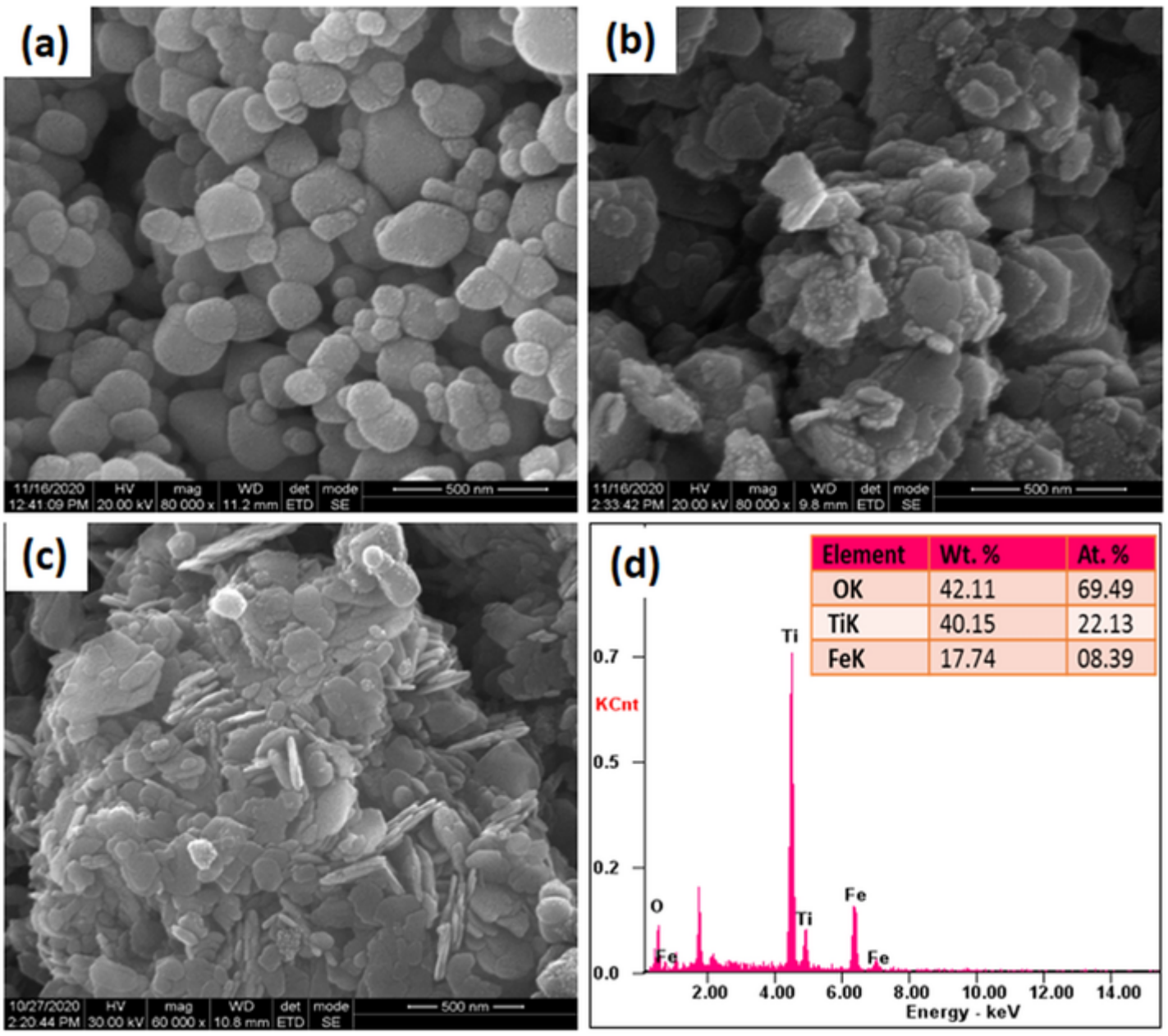

Fig. 4

EDX elemental distribution mapping of TiO_2/α-Fe_2O_3 composite; Pictures of **a** overall, **b** Ti, **c** Fe, and **d** O elements

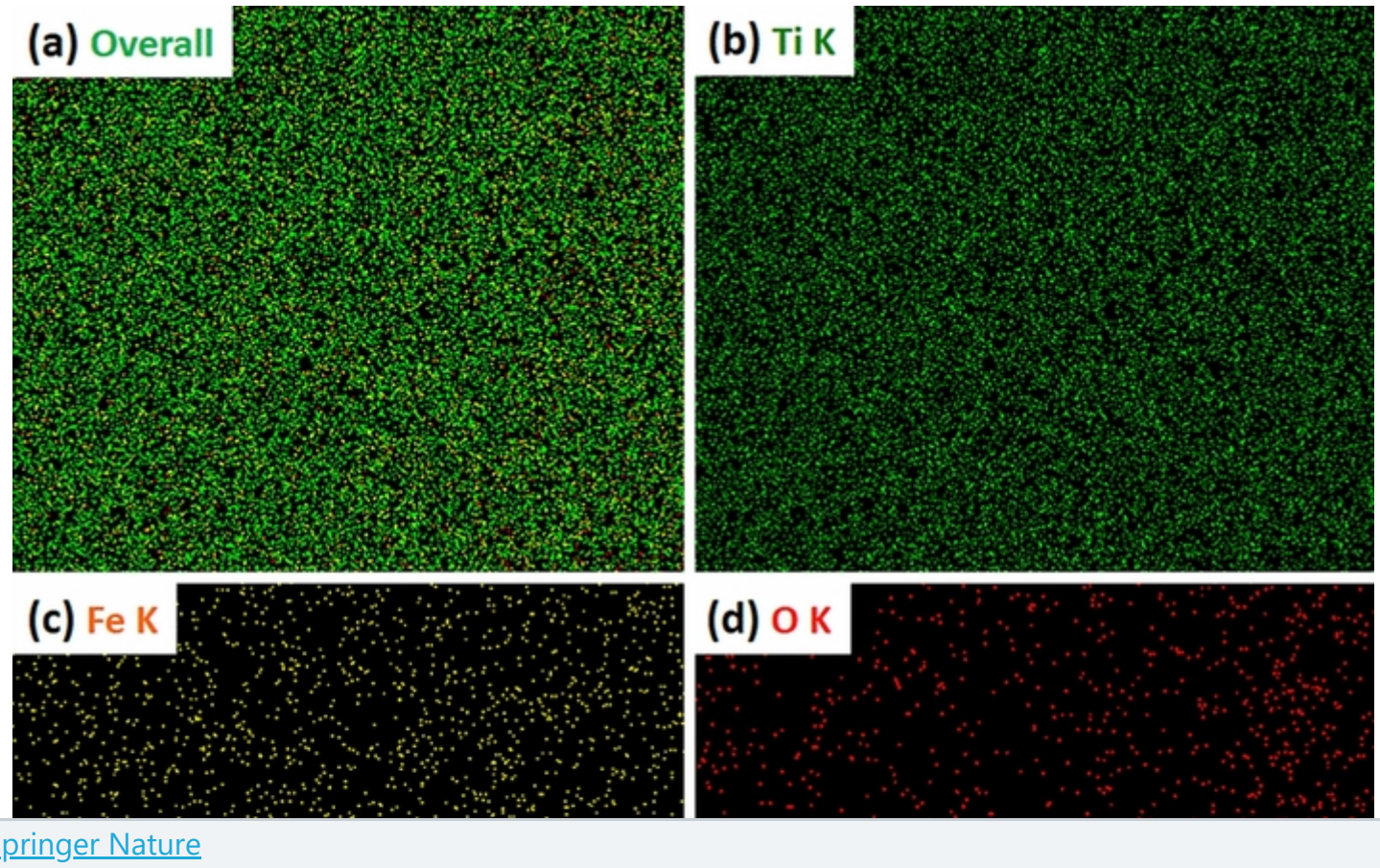

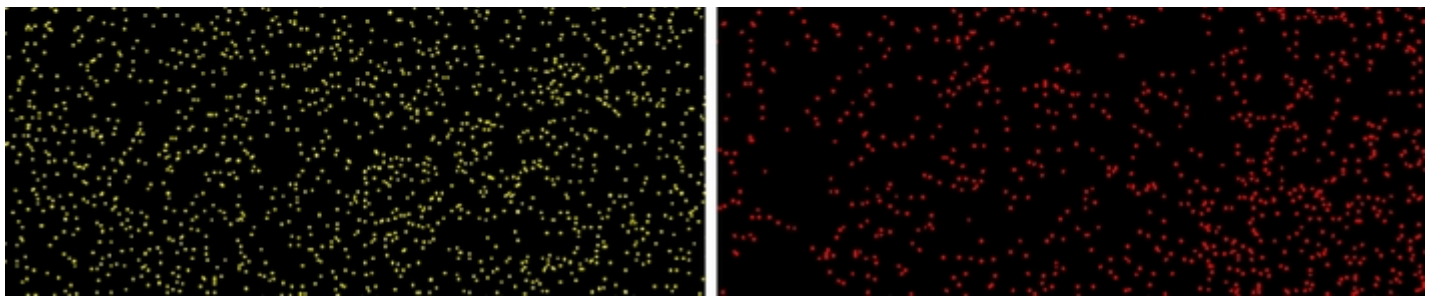

HRTEM images demonstrated that α-Fe_2O_3 NPs were uniformly distributed on the surface of TiO_2, as shown in Fig. 5 a–f. In addition, the characteristic HRTEM images further disclosed that the composite maintains flake-like structure with homogenous crumpled nanosheets [37]. The lattice fringes of as-prepared heterostructured TiO_2/α-Fe_2O_3 composite typically exposed to the (101) facets of TiO_2 and (012) crystallographic planes of α-Fe_2O_3 are discrete through measured the fringe spacing of 0.31 nm as presented in Fig. 5 e, f. Hence, the characteristic lattice lines for the selected area electron diffraction (SAED) pattern reveal the highly polycrystalline nature [6] of the obtained composite in Fig. 5 d. Also, Fig. 5 d confirms that the fruitful incorporation of both identical TiO_2 into α-Fe_2O_3 composite could be probable for the electrostatic interface among negatively charged TiO_2 and positively charged α-Fe_2O_3 NPs augmenting the charge carriers separation also notable for enlightened photocatalytic enrichment of TiO_2/α-Fe_2O_3 catalyst [38].

Fig. 5

Typical HRTEM images of as-fabricated TiO_2/α-Fe_2O_3 heterostructure composite

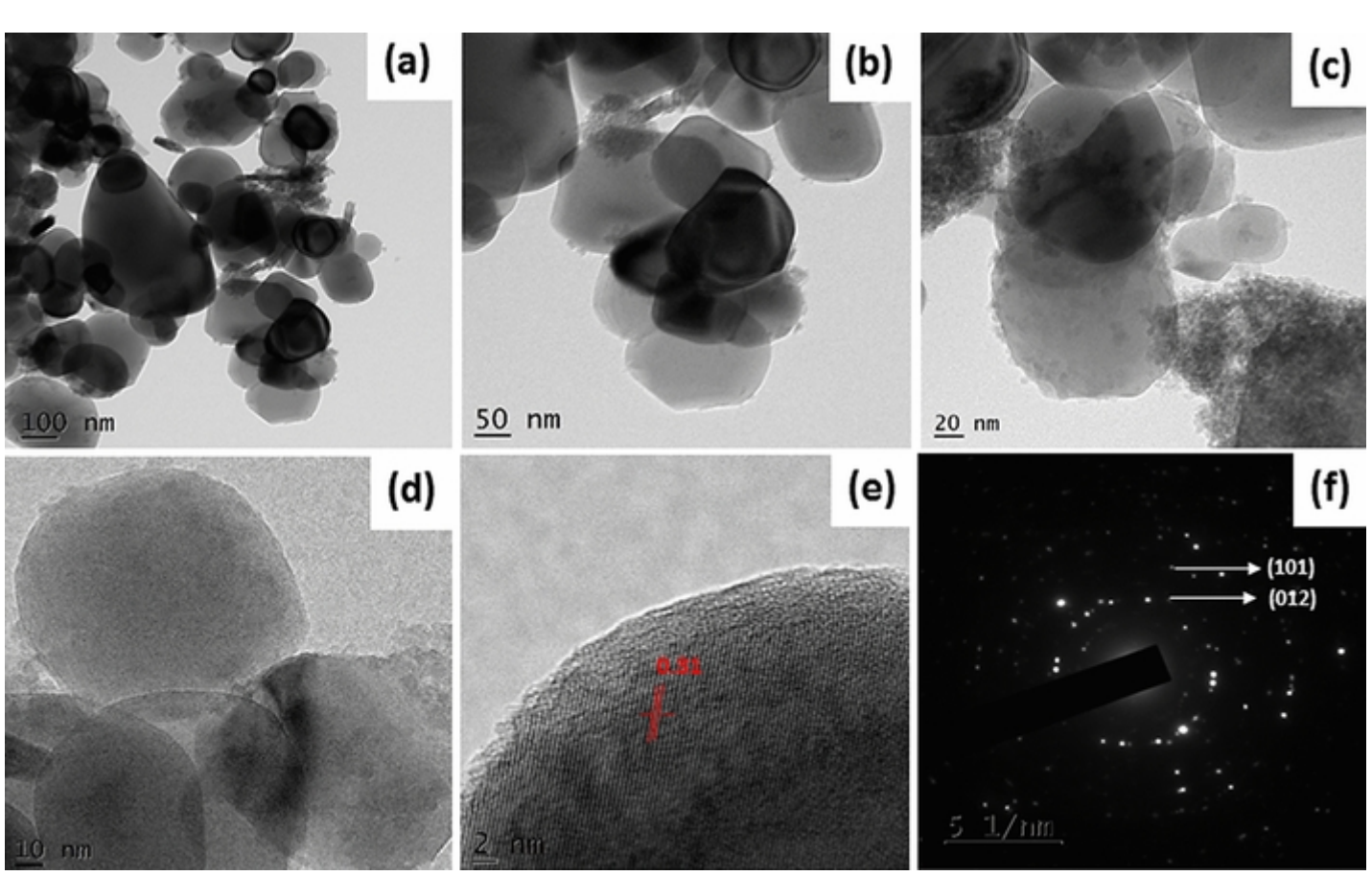

XPS study was employed to examine the chemical/oxidation states and surface compositions of the as-obtained TiO_2/α-Fe_2O_3 heterostructure. As exposed in Fig. 6 a–e, the α-Fe_2O_3/TiO_2 sample was composed of vital survey spectra, C 1 s, Ti 2p, O 1 s, and Fe 2p elemental core spectra, respectively. The high-resolution C1s XPS spectra (Fig. 6 b) is deconvoluted into three typical peaks that are 284.5, 285.2, and 288.9 eV. Also, the C 1 s spectra peak was ascribed to the adventitious hydro-carbon from the XPS instrument and/or PVP polymer-based carbon components. These active peaks could be related to C–O, C–C, and C–O=O, respectively. The typical strong peak of high-resolution Ti 2p XPS spectra (Fig. 6 c) was detected at 458.5 eV and 464.2 eV, which are agreed to the binding energies of Ti $2p_{3/2}$ and Ti $2p_{1/2}$ spin-orbiting splitting peaks, respectively. However, these binding energies were allotted to the Ti^{4+} form of TiO_2 NPs. **AQ1** Although the ~~three fitting peaks of~~ high-resolution XPS O 1 s spectra of three peaks (Fig. 6 d) are at 529.8 eV, 532.2 eV, and 533.1 eV, agreeing to the lattice oxygen, chemisorbed oxygen, and surface hydroxyl oxygen with metal-oxide linkages of Ti^{4+} and α-Fe_2O_3/TiO_2 NPs, respectively. Figure 6 e displays that the binding energies of Fe $2p_{3/2}$ and Fe $2p_{1/2}$ were situated at 711.4 eV and 722.6 eV, respectively; moreover, these peaks were ascribed to surface existed Fe offered in the Fe^{3+} formation of α-Fe_2O_3 phase. The shake-up satellite peak was noticed at about 719.5 eV in the Fe 2p elemental spectra. These outcomes are in good contract with the observed powder XRD result. Hence, these high-resolution XPS spectra outcomes have further established that the α-Fe_2O_3/TiO_2 heterostructured composite PCs were produced effectively.

Fig. 6

The high-resolution XPS a survey spectra of the TiO_2/α-Fe_2O_3 composite **b** C 1 s spectrum, **c** Ti 2p spectrum, **d** O 1 s spectrum and **e** Fe 2p spectrum respectively

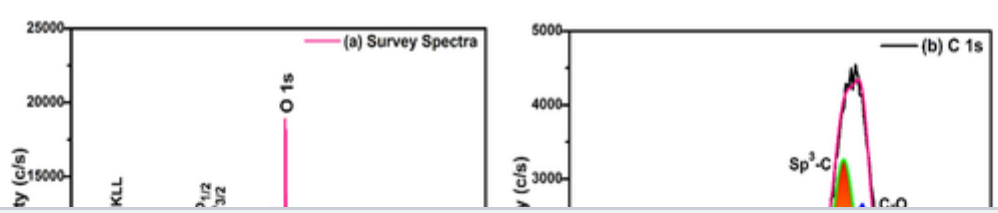

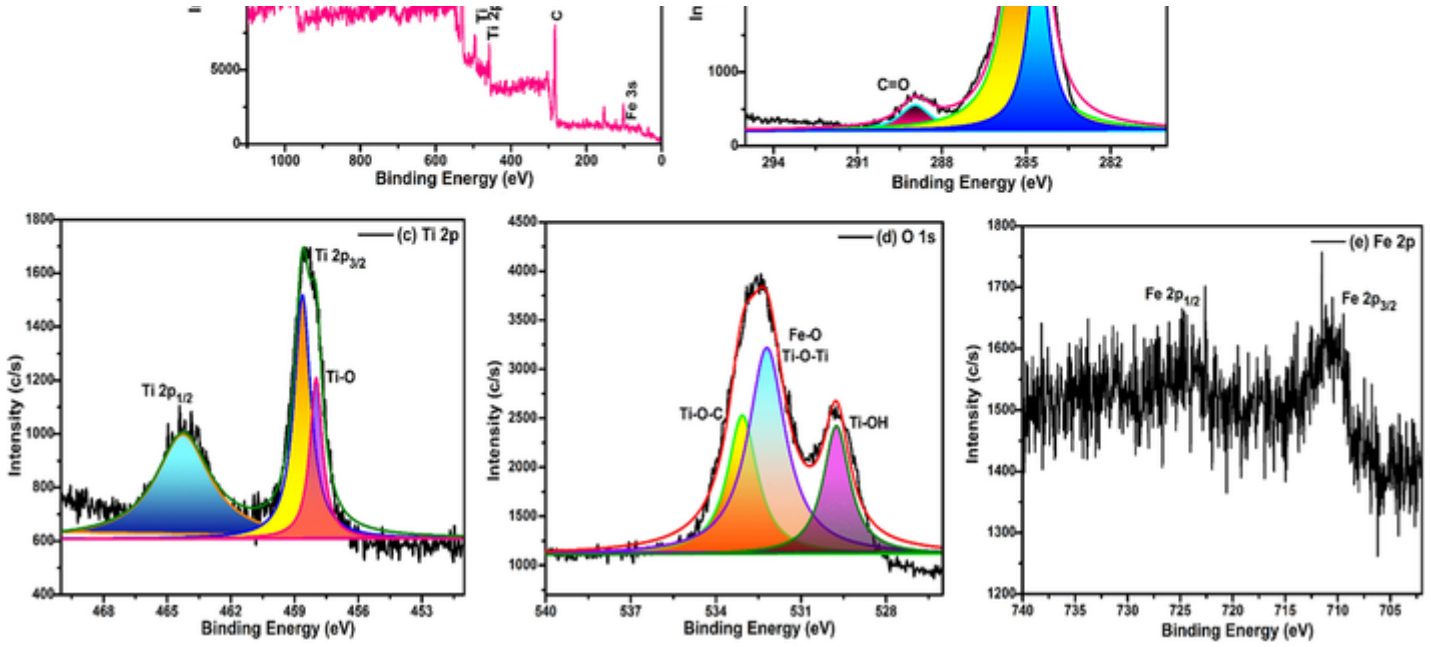

To check the visible-light response of as-prepared photocatalysts, UV–Vis DRS analysis was carried and the spectra are shown in Fig. 7 A. It could be seen that the UV–Vis absorption edge of pristine TiO_2 NPs is about ~ 325 nm in the spectra, whereas endorsed to the electronic transition of O_{2p} to Ti_{3d} [39], while pristine α-Fe_2O_3 NPs exhibits a wide visible-light absorption up to ~ 590 nm. Compared to bare TiO_2, the TiO_2/α-Fe_2O_3 spectrum shows a strong redshift, allowing to better use the UV and visible light for the photocatalytic oxidation (Fig. 7 A). The charge transfer by the direct transition from O2p to Fe^{3+} (3d) results in enhanced visible-light response to the elongated wavelength from the indirect transition among Fe^{3+} (3d) electrons (e^-) [29, 40]. **AQ2** **AQ3**

Fig. 7

A UV–Vis DRS spectra of as-prepared photocatalysts **B** relative Tauc plot of as-fabricated (a) pristine TiO_2, (b) α-Fe_2O_3, and (c) TiO_2/α-Fe_2O_3 NMs

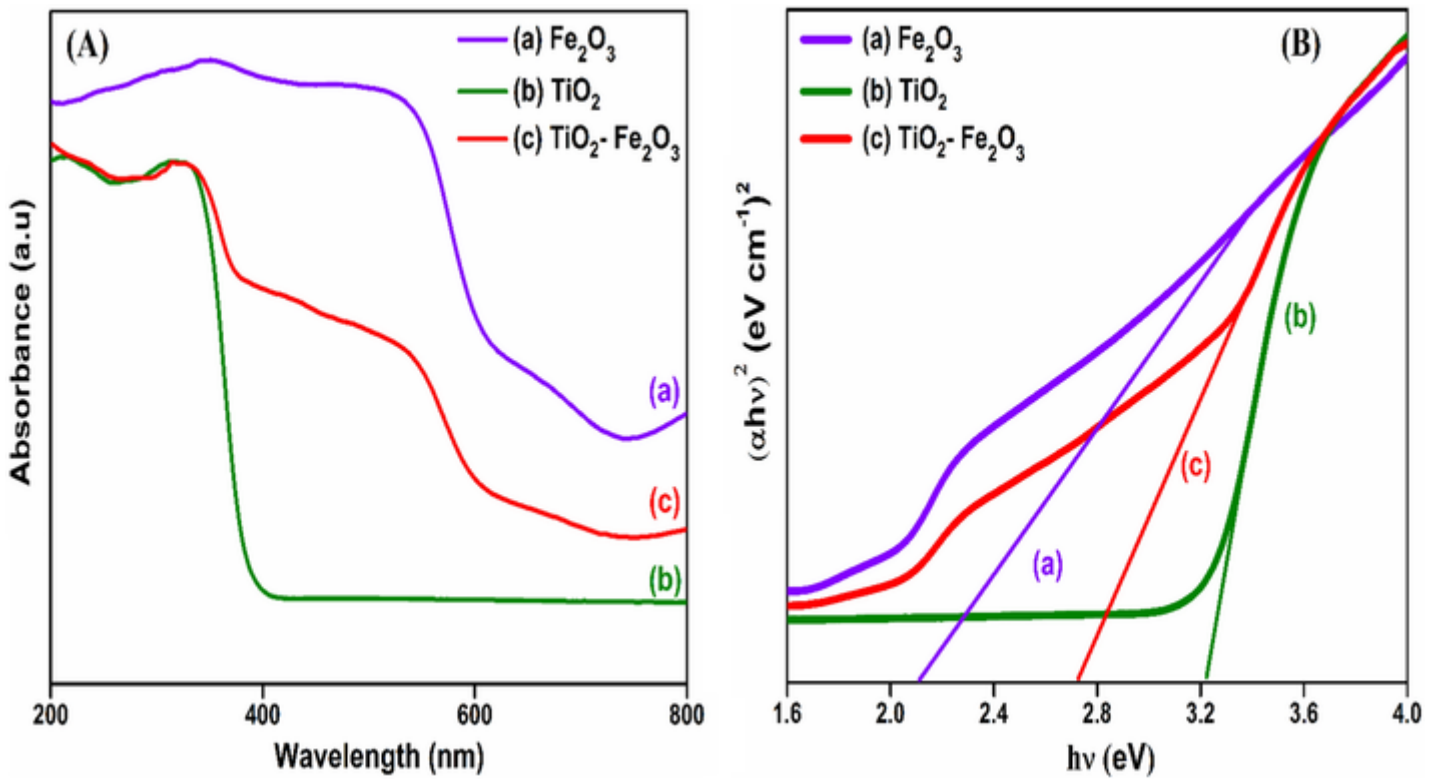

Figure 7 B illustrates the Tauc plots of $(\alpha h\nu)^2$ versus photon energy ($h\nu$) for the optical band-gap energies of as-attained catalysts, which intended founded on the optical absorption edge attained from UV–Vis DRS spectra using Kubelka-Munk Eqn: $\alpha h\nu = A\,(h\nu\, E_g)^{n/2}$, wherever, A, E_g, α, h, and v are the relatively constant, band-gap energy, absorption coefficient, Planck's constant, and incident light frequency, and where, n = ½, and 2 for direct and indirect band gap consistently [35]. These results show that the intercepts of band-gap energies of pristine TiO_2, α-Fe_2O_3, and TiO_2/α-Fe_2O_3 PCs are estimated to be 3.21, 2.11, and 2.72 eV, respectively. Decreased TiO_2/α-Fe_2O_3 is the main factor for enhanced photoactivity under visible light, which encourage the use of solar light in real conditions [41]. The photoactivity under visible light could be due to two main mechanisms: α-Fe_2O_3 can play the role of visible-light-responsive photocatalyst and also photosensitizer for TiO_2, wherein, the photoexcited carriers can be transferred to TiO_2; (ii) Fe^{3+} species could be inserted in TiO_2 lattice and forms novel mi-gap allowing the excitation of TiO_2 with visible light [42]. Based on the UV–Vis DRS results, the as-fabricated TiO_2/α-Fe_2O_3 PCs was narrowed optical band gap and high visible-light utilization ability, thus, the photocatalytic enhancing performance for decomposing organic impurities [1].

PL emission spectra were carried out to explore the efficiency of photo-produced (e^-/h^+) pairs, transfer, separation, trapping, immigration, and to understand the rate of charge-carrier recombination in the specified semiconductor PCs one of the essential factors affecting the photocatalytic properties. Figure 8 A shows the PL spectra of as-prepared heterostructured PCs, wherein the emission intensity peaks of the as-fabricated pristine TiO_2, α-Fe_2O_3, and TiO_2/α-Fe_2O_3 photocatalysts were at 461, 447, and 459 nm, respectively. The PL emission peak of TiO_2 was upper than that of TiO_2/α-Fe_2O_3 composite, which designated that occurrence of α-Fe_2O_3 reduced the (e^-/h^+) recombination rate [43]. In contrast, novel configurations of the heterostructure among α-Fe_2O_3 and TiO_2 NMs decline the PL emission intensity of the near-band edge emission (NBE) and might be owed to the intrinsic/extrinsic luminescence defects related to NBE. The Fe^{3+}/ Fe_2O_3 ions

interstitial of Fe^{3+}. So the lesser PL emission intensity of the TiO_2/α-Fe_2O_3 PCs has significance in charge separation that specifies the effectively restrained recombination rate primary to admirable light-harvesting capability; hence, the photocatalytic efficacy was heightened [30].

Fig. 8

A Room-temperature PL spectra, $\lambda_{ex} \sim 330$ nm; and **B** photocatalytic degradation of MB over the TiO_2/α-Fe_2O_3 composite catalyst under visible-light exposure

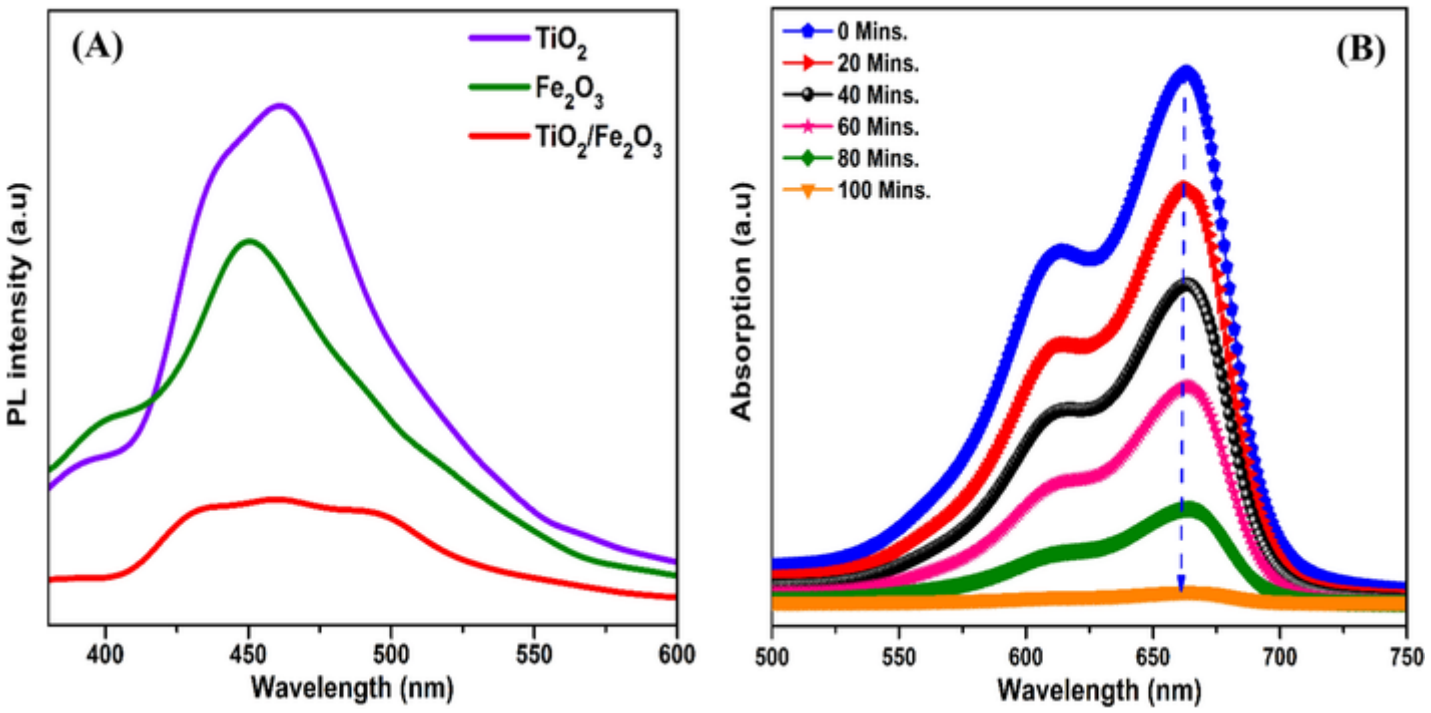

3.1. Photocatalytic activity

The photocatalytic activities of as-prepared photocatalysts were comparatively evaluated towards the oxidation of MB under visible light. Figure 8 B shows the decrease of MB absorbance during photocatalytic oxidation using TiO_2/α-Fe_2O_3 within 100 min. Also, the results showed that the self-degradation of MB aqueous solution without photocatalyst (blank), and the dark adsorption of MB on the surface of the photocatalysts were negligible. The MB photodegradation efficacy over TiO_2 and α-Fe_2O_3 was only 33 and 47. %, respectively. Moreover, the TiO_2/α-Fe_2O_3 heterostructured composite catalyst shows the highest photocatalytic activity (92.7%) within 100 min under visible-light irradiation. Figure 9 A demonstrates the consistent concentration changes of the MB aqueous dye solution and the response rate (k) as a function of visible-light exposure time [38, 40]. The photodegradation performance of the blank test for the as-obtained photocatalyst samples towards the MB aqueous dye solution was calculated under similar conditions as shown in Fig. 9 A. For the blank tests (without any photocatalyst), which only a little change with the extension of light exposure [44], signifying that the photolysis of MB aqueous dye molecules is very weak. However, the photodegradation behaviors of MB dye without the light exposure leading of PCs was also tested for comparison [45].

Fig. 9

A Photodegradation efficiency of MB dye. **B** First-order kinetic fitting plots − ln (C_0/C_t) versus reaction time t for the as-obtained different PCs

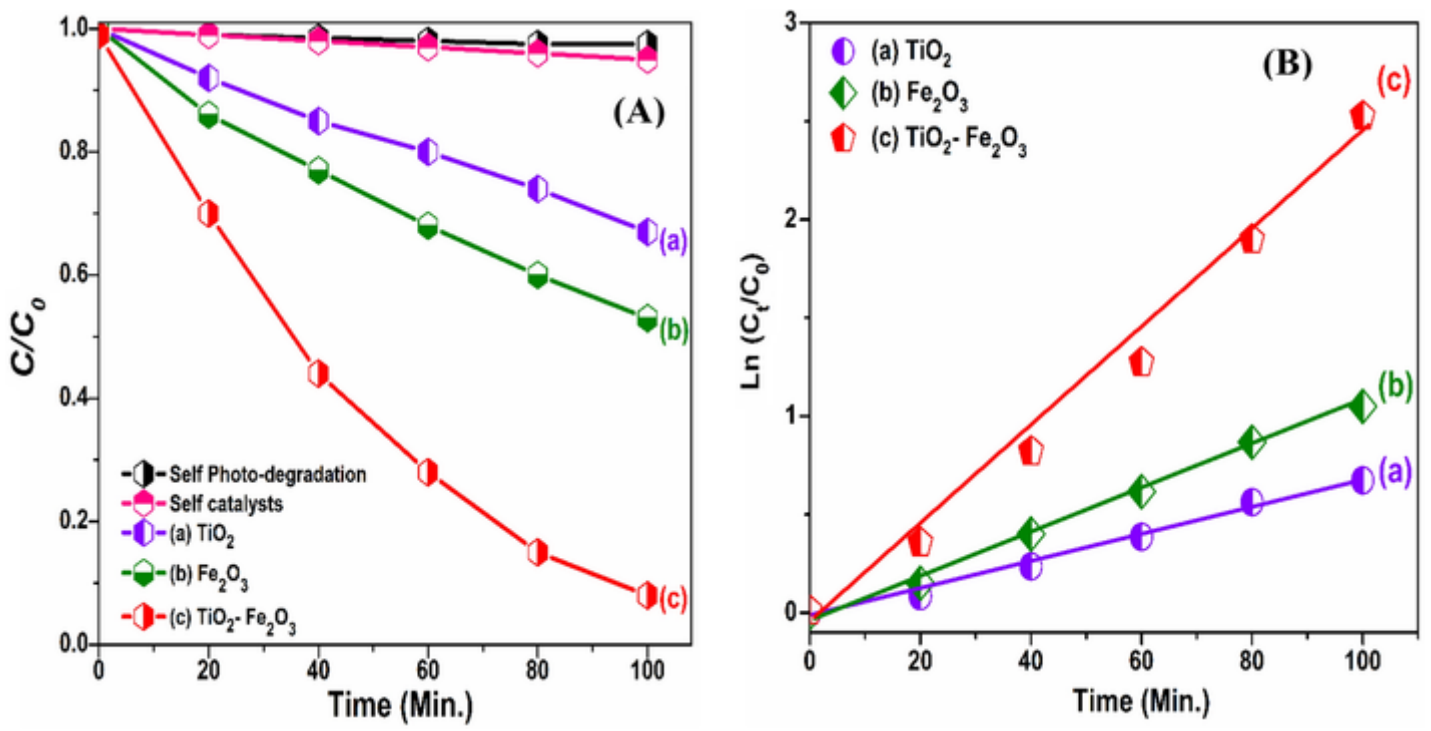

Figure 9 B shows that the photocatalytic oxidation of MB over different photocatalysts follows pseudo-first-order kinetics. The reaction rate constants (k) for were found to be 0.0071 min^{-1}, 0.0109 min^{-1}, and 0.0252 min^{-1} for TiO_2, α-Fe_2O_3, and TiO_2/α-Fe_2O_3 PCs, respectively. It was found that TiO_2/α-Fe_2O_3 exhibits a better photocatalytic performance of 3.54 and 2.31 times greater than those of bare TiO_2 and α-Fe_2O_3 under the same conditions, respectively. Besides photocatalytic efficacy, the stability of the specified photocatalyst is also essential for practical use for the handling of organic pollutants in wastewaters [46]. TiO_2/α-Fe_2O_3 was reused five successive times

under the same conditions, and after the results are shown in Fig. 10 A. It can be seen that TiO_2/α-Fe_2O_3 showed good recycling effectiveness five times without notable loss in the photocatalytic efficiency, suggesting good stability. However, the slight decrease after the fifth use (80.6%) might be due to the loss of TiO_2/α-Fe_2O_3 catalyst during recycling. The crystalline structure and their functional groups were characterized by XRD and FT-IR to check the stability of the photocatalyst after recycling [40]. It can be seen that TiO_2/α-Fe_2O_3 PCs have almost no obvious structural changes after the photocatalytic recycles investigations (Fig. 11 A, B) which suggests good stability. In contrast, it is important to point out, with the previous recent reported literature of various NCs for photodegradation of organic impurities, TiO_2/α-Fe_2O_3 composite PCs have displayed superb removal efficacy for MB dye, as tabularized in Table 1.

Fig. 10

A Recycling stability of energetic TiO_2/α-Fe_2O_3 PCs and **B** photodegradation of MB aqueous dye over TiO_2/α-Fe_2O_3 composite catalyst in the existence of ROSs scavengers

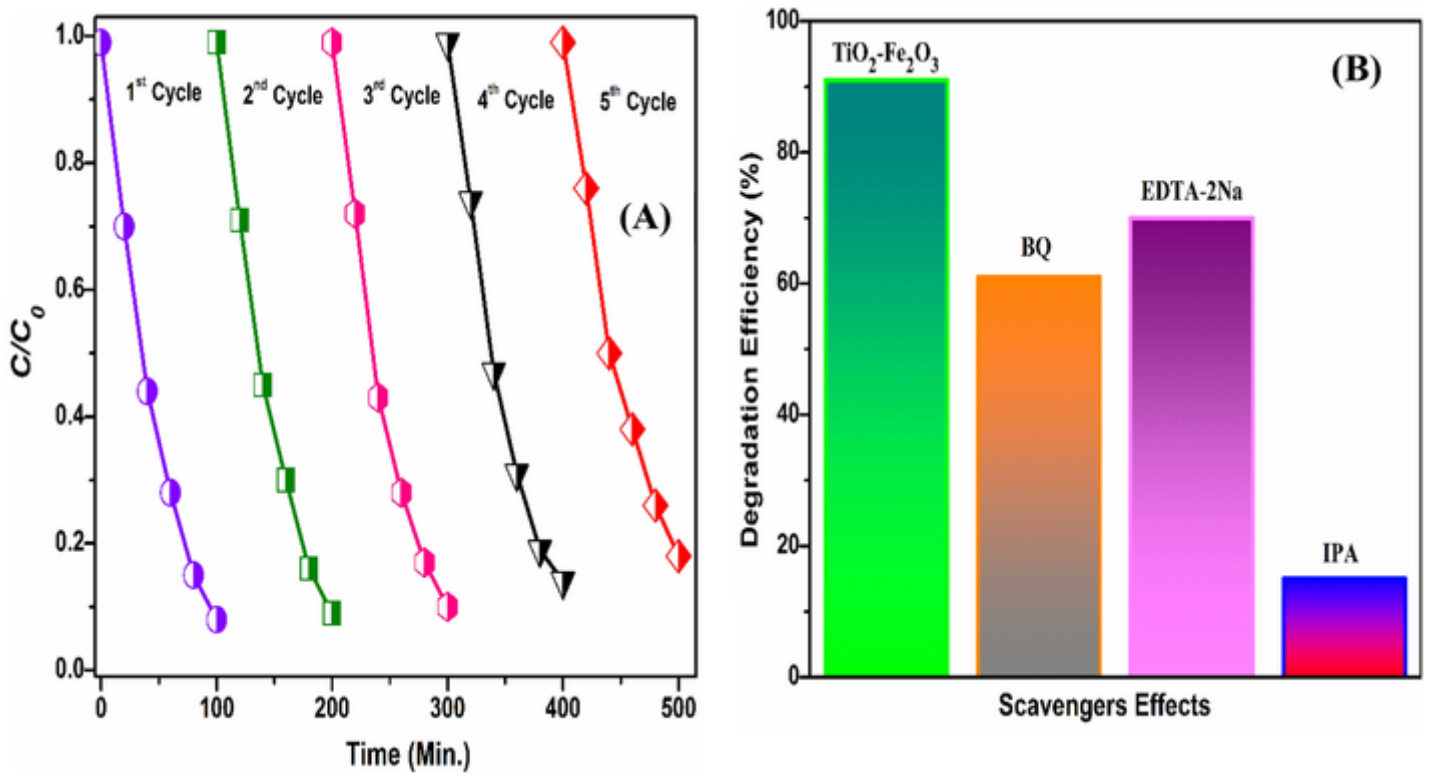

Fig. 11

A XRD pattern and **B** FT-IR spectra of TiO_2/α-Fe_2O_3 composite catalyst before (a) and after (b) recycling

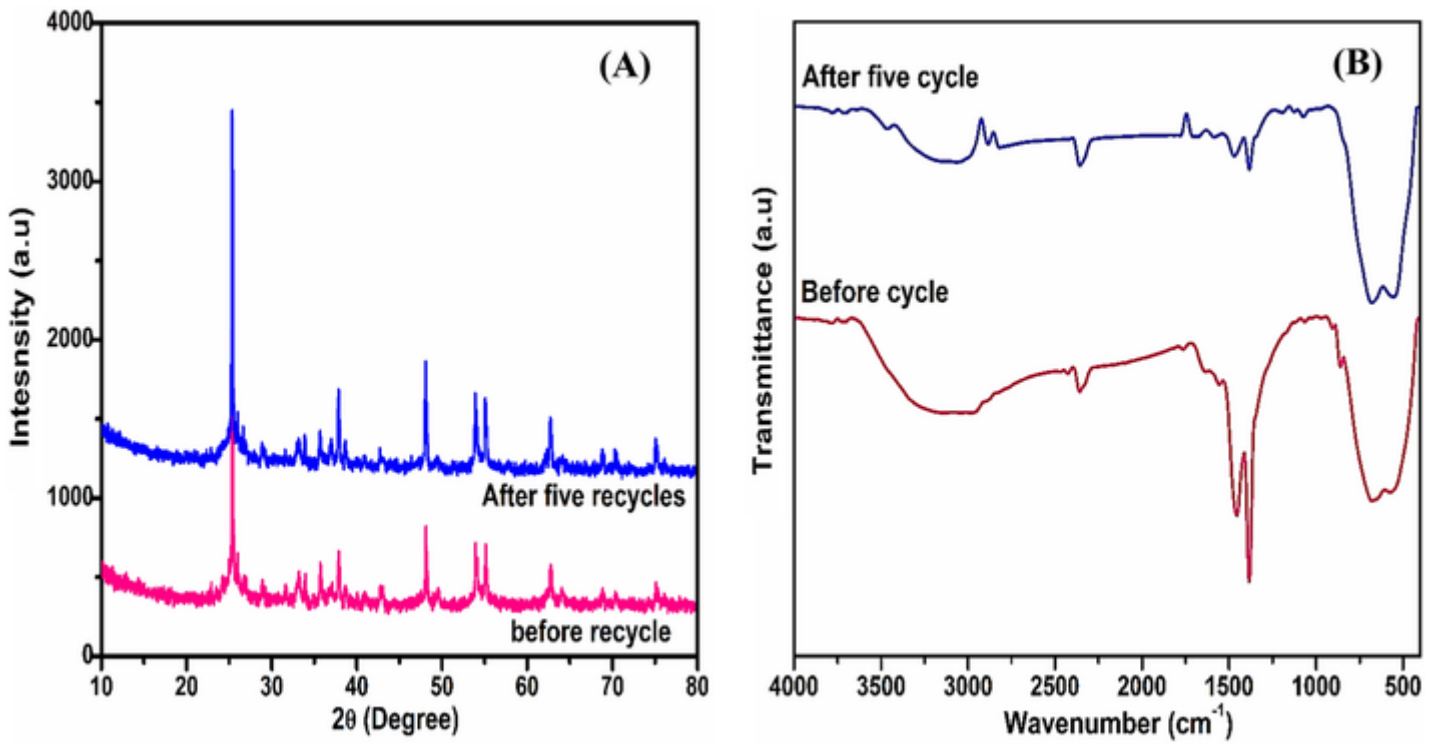

Table 1

Comparison of VLD photocatalytic degradation of MB dye (%) over previous reported photocatalytic NMs

Photocatalyst/L		MB dye concentration	Irradiation time (min.)	Degradation efficiency (%)	Ref.
Ga-Ag/ZnO	10 mg	6 mg/L	300	~ 39	[47]
P25 TiO_2	2 mg	20 mg/L	300	~ 48	[48]
CNTs/TiO_2/Ag	20 mg	5 mg/L	240	~ 48	[2]
ZnO/SnO_2	10 mg	3 mg/L	240	~ 90	[49]
TiO_2/CeO_5	100 mg	40 mg/L	150	~ 95	[46]
CdS/TiO_2	50 mg	15 mg/L	180	~ 63	[26]
Fe$_2$O$_3$/Cu$_2$O	30 mg	10 mg/L	80	~ 40	[50]

Photocatalyst/L		MB dye concentration	Irradiation time (min.)	Degradation efficiency (%)	Ref.
TiO_2/α-Fe_2O_3	50 mg	20 mg/L	100	~ 92.7	This work

The scavenging agents for different reactive oxygen species were used to prove the photocatalytic radical oxidation ability of TiO_2/α-Fe_2O_3 (Fig. 10 B). Three quenching agents such as 0.5 mM of isopropanol (IPA), disodium ethylene diamine-tetra acetate (EDTA-2Na), and benzoquinone (BQ) are to trap hydroxyl radicals ($^{\bullet}OH$), holes (h^+) and superoxide anion radicals ($^{\bullet}O_2-$), respectively [43]. As shown in Fig. 10 B, the decomposition rate of PCs slightly decreased while the addition of BQ and EDTA-2Na shows that the h^+ and $^{\bullet}O_2-$ species are not major responsive species on the photocatalytic system [51]. Nevertheless, the addition of IPA results in strong inhibition of the photocatalytic oxidation of MB wherein the oxidation rate declined from 92.7 to 16%. This result indicates the main role of $^{\bullet}OH^-$ radicals produced by TiO_2/α-Fe_2O_3 under visible light towards the oxidation of MB dye.

Based on the obtained results, it is noticeable that the generation of separated (e^--h^+) in the TiO_2/α-Fe_2O_3 system could lead to enhanced radical oxidation under visible light [30]. The VB and CB edge potential position could be gathered according to the Mulliken electronegativity theory for the following equation: $E_{VB} = \chi - E_e + 0.5\,E_g$ and $E_{CB} = E_{VB} - E_g$, wherein χ signifies the absolute Mulliken electronegativity of given SCs (χ-TiO_2 = 5.81 eV, and χ α-Fe_2O_3 = 5.88 eV) [52]. Moreover, the E_g, E_e, E_{VB}, and E_{CB} were energy band gap of specified SCs by UV-DRS spectra (E_g of TiO_2 = 3.21 eV; E_g of α-Fe_2O_3 = 2.11 eV), the energy of free electrons on the hydrogen scale (ca. 4.5 eV), VB edge potential, and CB edge potential individually [53]. Agreeing to the above equations, the energy-level diagram is based upon the E_{VB} and E_{CB} values that were estimated to be of TiO_2 (E_{VB} = 2.915, E_{CB} = − 0.295) and it is favorable than α-Fe_2O_3 (E_{VB} = 2.48, E_{CB} = 0.28).

Based on the above results and discussion, the photo-produced charge separation and transfer of the TiO_2/α-Fe_2O_3 heterostructure catalyst for the improved plausible photocatalytic action in visible-light preservation could be anticipated as shown in Fig. 12. Under the visible-light illumination ($\lambda > 420$ nm), both the catalysts are excited by energetic photons while producing the more electron–hole (e^--h^+) pairs, which are then separated and stimulated to diverse ways under the reaction energy [35]. In detail, the photo-electrons (e^-) of TiO_2 will transfer to the CB of α-Fe_2O_3, meanwhile, the photo-holes (h^+) of α-Fe_2O_3 will transport to the VB of TiO_2 (Ti 3d) under the exploit of a built-in electric field. However, under the energetic reaction, the photo-electrons (e^-) of α-Fe_2O_3 and the photo-holes (h^+) of TiO_2 would exchange to both other and then concluding the consequence of (e^--h^+) recombination. In photocatalytic system, the photo-electrons (e^-) prompt to the reduction of Fe^{3+} ions to Fe^{2+} ions [50]. When α-Fe_2O_3 NPs were united with TiO_2 NPs, the Fermi levels of TiO_2 and α-Fe_2O_3 necessity align in symmetry owing to the occurrence of the TiO_2/α-Fe_2O_3 heterojunction [29]. The authority of TiO_2/α-Fe_2O_3 NSs also profits from the pairing by narrow band-gap semiconductor α-Fe_2O_3. Thus, the (e^-/h^+) recombination progression is greatly suppressed, and efficient (e^-/h^+) separation is realized on the composite surface [48]. In this case, the presence of TiO_2/α-Fe_2O_3-fitted heterostructures, the conversion of the photo-electrons (e^-) and the photo-holes (h^+) would primarily go through the hybrid layer simply owed the firm migration rate position which also stimulates the outstanding charge separation movement. Concurrently, the samples of TiO_2 and α-Fe_2O_3 PCs will initiate redox reactions in the medium to produce different ROSs for the oxidation of organic pollutants. Also, the photo-electrons (e^-) in the CB was auxiliary respond with molecular oxygen O_2 dissolved in the solution to form the superoxide anion ($O_2^{\bullet-}$) and hydrogen peroxide (H_2O_2). Positive holes in the VB are able to generate $^{\bullet}OH$ from the oxidation of ^-OH or H_2O. Consecutively, the photodegradation of MB dye could be achieved via the direct oxidation by positive holes or via the photo-produced ROSs oxidation [36] as shown in Fig. 12. The decrease of the recombination rate also due to the separation of photo-produced charges at the interface of TiO_2/α-Fe_2O_3 could be one of the reasons behind the enhanced photoactivity in [54, 55].

Fig. 12

Schematic diagram for the photocatalytic mechanisms of MB dye over the surface of TiO_2/α-Fe_2O_3 heterostructure composite under visible-light irradiation

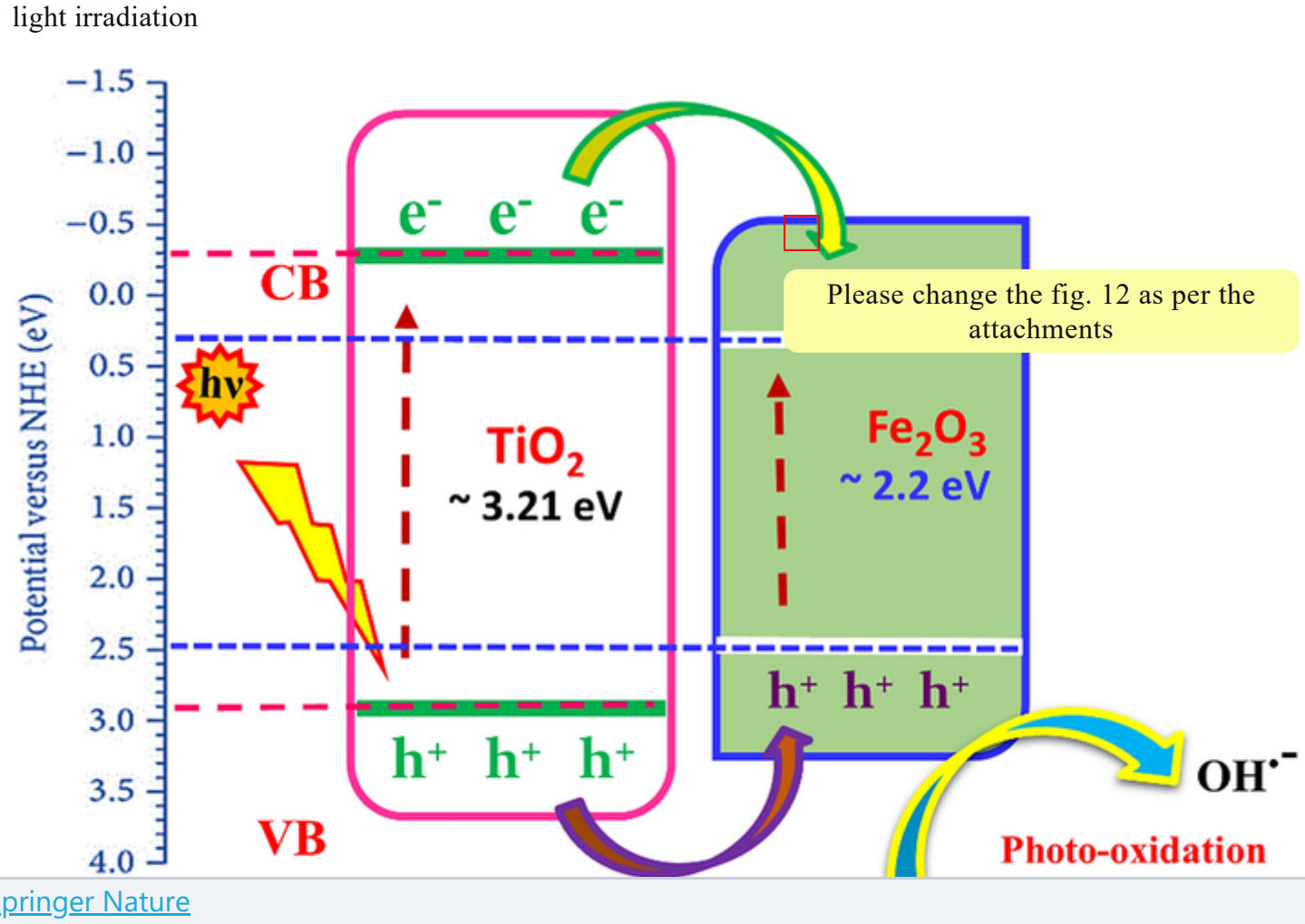

4. Conclusions

In summary, a visible-light-responsive TiO_2/α-Fe_2O_3 was fabricated via the combination of TiO_2 (synthesized by hydrothermal route) and α-Fe_2O_3 (obtained via precipitation). The powder XRD diffraction pattern peaks of TiO_2 and α-Fe_2O_3 NPs well accorded with the tetragonal (anatase) and rhombohedral phases obtained. The narrow band gap of α-Fe_2O_3 was engaged to outspread the optical response of TiO_2 to the visible-light region. AQ4 Although, the TiO_2/α-Fe_2O_3 sample has revealed ~~the~~ for premier photocatalytic action of the organic MB aqueous dye among the bare as-fabricated TiO_2 and α-Fe_2O_3 PCs ~~in the~~ under visible-light region. TiO_2/α-Fe_2O_3 also exhibits an adequate superior cyclic stability wherein the decomposition efficiency was found to be 80.6% at the fifth recycling run. It is claimed that the well-suited interface fashioned heterojunction structures between TiO_2 and α-Fe_2O_3 are the reason behind the enhanced photogeneration and separation of e^--h^+ charges, restraining the recombination rate, which boosts the generation of ROSs. To conclude, a promising photocatalytic mechanism was suggested to describe the photocatalytic oxidation of MB over TiO_2/α-Fe_2O_3 under visible light. TiO_2/α-Fe_2O_3 showed great potential for the photocatalytic oxidation of organic pollutants in water. AQ5 AQ6

Publisher's Note

Acknowledgements

The authors extend their thanks to Research Supporting Project (Ref: RSP-2021/160) King Saud University.

Declarations

Conflict of interest The authors have declared no conflict of interest.

References

1. G.K. Upadhyay, J.K. Rajput, T.K. Pathak, V. Kumar, L.P. Purohit, Vacuum **160**, 154 (2019)

2. Y. Koo, G. Littlejohn, B. Collins, Y. Yun, V.N. Shanov, M. Schulz, D. Pai, J. Sankar, Compos. Part B: Eng. **57**, 105 (2014)

3. S. He, P. Hou, E. Petropoulos, Y. Feng, Y. Yu, L. Xue, L. Yang, Front. Chem. **6**, 1 (2018)

4. M. Wang, Y. Hu, J. Han, R. Guo, H. Xiong, Y. Yin, J. Mater. Chem. A **3**, 20727 (2015)

5. L. Kong, J. Yan, P. Li, S.F. Liu, ACS Sustain. Chem. Eng. **6**, 10436 (2018)

6. G.R. Surikanti, A.K. Bandarapu, M.V. Sunkara, ChemistrySelect **4**, 2249 (2019)

7. P. Pooseekheaw, W. Thongpan, A. Panthawan, E. Kantarak, W. Sroila, P. Singjai, Molecules **25**, 3327 (2020)

8. W.K. Jo, T. Adinaveen, J.J. Vijaya, N.C. Sagaya Selvam, RSC Adv. **6**, 10487 (2016)

9. A. Leelavathi, B. Mukherjee, C. Nethravathi, S. Kundu, M. Dhivya, N. Ravishankar, G. Madras, RSC Adv. **3**, 20970 (2013)

10. J. Sun, X. Li, Q. Zhao, J. Ke, D. Zhang, J. Phys. Chem. C **118**, 10113 (2014)

11. M.S.S. Danish, A. Bhattacharya, D. Stepanova, A. Mikhaylov, M.L. Grilli, M. Khosravy, T. Senjyu, Metals **10**, 1 (2020)

12. W.K. Jo, N. Clament Sagaya Selvam, J. Hazard. Mater. **299**, 462 (2015)

13. S. Martha, P. Chandra Sahoo, K.M. Parida, RSC Adv. **5**, 61535 (2015)

14. C. Karthikeyan, P. Arunachalam, K. Ramachandran, A.M. Al-Mayouf, S. Karuppuchamy, J. Alloy. Compd. **828**, 154281 (2020)

15. S. Gautam, H. Agrawal, M. Thakur, A. Akbari, H. Sharda, R. Kaur, M. Amini, J. Environ. Chem. Eng. **8**, 103726 (2020)

16. A. Gołąbiewska, M.P. Kobylański, A. Zaleska-Medynska, *Metal Oxide-Based Photocatalysis: Fundamentals and Prospects for Application* (Elsevier, Amsterdam, 2018), pp. 3–50

17. M.M. Mohamed, W.A. Bayoumy, M.E. Goher, M.H. Abdo, T.Y. Mansour El-Ashkar, Appl. Surf. Sci. **412**, 668 (2017)

18. W.K. Jo, N.C.S. Selvam, Dalton Trans. **44**, 16024 (2015)

19. L. Xu, J. Wang, Environ. Sci. Technol. **46**, 10145 (2012)

20. S. Balu, S. Velmurugan, S. Palanisamy, S.W. Chen, V. Velusamy, T.C.K. Yang, and E. S. I. El-Shafey. J. Taiwan Inst. Chem. Eng. **99**, 258 (2019)

21. R. Djellabi, B. Yang, H.M. Adeel Sharif, J. Zhang, J. Ali, X. Zhao, J. Clean. Prod. **233**, 841 (2019)

22. L. Baia, E. Orbán, S. Fodor, B. Hampel, E.Z. Kedves, K. Saszet, I. Székely, É Karácsonyi, B. Réti, P. Berki, A. Vulpoi, K. Magyari, A. Csavdári, C. Bolla, V. Coşoveanu, K. Hernádi, M. Baia, A. Dombi, V. Danciu, G. Kovács, Z. Pap, Mater. Sci. Semicond. Process. **42**, 66 (2016)

23. A.M. Abdel-Wahab, A.S. Al-Shirbini, O. Mohamed, O. Nasr, J. Photochem. Photobiol. A **347**, 186 (2017)

24. M.R.A. Kumar, B. Abebe, H.P. Nagaswarupa, H.C.A. Murthy, C.R. Ravikumar, F.K. Sabir, Sci. Rep. **10**, 1249 (2020)

25. S. Ma, S. Zhan, Y. Jia, Q. Zhou, ACS Appl. Mater. Interfaces **7**, 10576 (2015)

26. H. Wei, L. Wang, Z. Li, S. Ni, Q. Zhao, Nano-Micro Lett. **3**, 6 (2011)

27. K. Kaviyarasan, V. Vinoth, T. Sivasankar, A.M. Asiri, J.J. Wu, S. Anandan, Ultrason. Sonochem. **51**, 223 (2019)

28. D. He, Y. Yang, J. Tang, K. Zhou, W. Chen, Y. Chen, Z. Dong, Environ. Sci. Pollut. Res. **26**, 12359 (2019)

29. X. Lu, X. Li, F. Chen, Z. Chen, J. Qian, Q. Zhang, J. Alloy. Compd. **815**, 152326 (2020)

30. J. Tian, P. Hao, N. Wei, H. Cui, H. Liu, ACS Catal. **5**, 4530 (2015)

31. R.M. Cornell, U. Schwertmann, *The Iron Oxides* (Wiley, Hoboken, 2003)

32. R. Djellabi, B. Yang, K. Xiao, Y. Gong, D. Cao, H.M.A. Sharif, X. Zhao, C. Zhu, J. Zhang, J. Colloid Interface Sci. **553**, 409 (2019)

33. R. Djellabi, X. Zhao, C.L. Bianchi, P. Su, J. Ali, B. Yang, J. Clean. Prod. **269**, 122286 (2020)

34. M. Fakhrul Ridhwan Samsudin, S. Sufia, R. Bashiri, N. Muti Mohamed, L.T. Siang,, R.M. Ramli, Mater. Today: Proc. **5**, 21710 (2018)

35. W.A. Aboutaleb, R.A. El-Salamony, Mater. Chem. Phys. **236**, 121724 (2019)

36. L. Zhu, H. Li, Z. Liu, P. Xia, Y. Xie, D. Xiong, J. Phys. Chem. C **122**, 9531 (2018)

37. S. Chandrasekaran, W.M. Choi, J.S. Chung, S.H. Hur, E.J. Kim, Mater. Lett. **136**, 118 (2014)

38. V. Ramasamy Raja, A. Karthika, S. Lok Kirubahar, A. Suganthi, M. Rajarajan, Solid State Ionics **332**, 55 (2019)

39. D. Lu, B. Zhao, P. Fang, S. Zhai, D. Li, Z. Chen, W. Wu, W. Chai, Y. Wu, N. Qi, Appl. Surf. Sci. **359**, 435 (2015)

40. N.S. Arul, D. Mangalaraj, R. Ramachandran, A.N. Grace, J.I. Han, J. Mater. Chem. A **3**, 15248 (2015)

41. B. Sharma, P.K. Boruah, A. Yadav, M.R. Das, J. Environ. Chem. Eng. **6**, 134 (2018)

42. J. Qin, C. Yang, M. Cao, X. Zhang, R. Saravanan, S. Limpanart, M. Ma, R. Liu, Mater. Lett. **189**, 156 (2017)

43. L. Rožić, S. Petrović, D. Lončarević, B. Grbić, N. Radić, S. Stojadinović, V. Jović, J. Lamovec, Ceram. Int. **45**, 2361 (2019)

44. C.V. Reddy, B. Babu, J. Shim, J. Phys. Chem. Solids **112**, 20 (2018)

45. D. Ke, H. Liu, T. Peng, X. Liu, K. Dai, Mater. Lett. **62**, 447 (2008)

46. J.C. Cano-Franco, M. Álvarez-Láinez, Mater. Sci. Semicond. Process. **90**, 190 (2019)

47. M.N. Cardoza-Contreras, A. Vásquez-Gallegos, A. Vidal-Limon, J.M. Romo-Herrera, S. Águila, O.E. Contreras, Catalysts **9**, 1 (2019)

48. M. Gurulakshmi, M. Selvaraj, A. Selvamani, P. Vijayan, N.R. Sasi, Rekha, K. Shanthi, Appl. Catal. A **449**, 31 (2012)

49. M.M. Rashad, A.A. Ismail, I. Osama, I.A. Ibrahim, A.H.T. Kandil, Arabian J. Chem. **7**, 71 (2014)

50. S.K. Lakhera, R. Venkataramana, A. Watts, M. Anpo, B. Neppolian, Res. Chem. Intermed. **43**, 5091 (2017)

51. A.B. Ali Baig, V. Rathinam, V. Ramya, Mater. Technol. **36**, 623 (2021)

52. R. Saravanan, V.K. Gupta, E. Mosquera, F. Gracia, J. Mol. Liq. **198**, 409 (2014)

53. D. Zhang, S. Cui, J. Yang, J. Alloy. Compd. **708**, 1141 (2017)

54. R. Li, Y. Jia, N. Bu, J. Wu, Q. Zhen, J. Alloy. Compd. **643**, 88 (2015)

55. Z. Zhang, Y. Ma, X. Bu, Q. Wu, Z. Hang, Z. Dong, X. Wu, Sci. Rep. **8**, 10532 (2018)